THE JOURNAL OF PHYSICAL CHEMISTRY C
A JOURNAL OF THE AMERICAN CHEMICAL SOCIETY

pubs.acs.org/JPCC

Article

An Efficient and Durable Electrocatalyst Based on Strongly Coupled Pt Nanoparticles on CeO_2 Microspheres for CO-Resilient Methanol Oxidation

Paskalis Sahaya Murpin Kumar, Subramanian Arulmani, Hyoung-il Kim, Deepthi Koolath Ramakrishnan, Vinoth Kumar Ponnusamy, Umapada Pal, and Siva Kumar Krishnan*

Cite This: *J. Phys. Chem. C* 2022, 126, 18670−18682

Read Online

ACCESS | Metrics & More | Article Recommendations | Supporting Information

ABSTRACT: Designing durable, highly active supported Pt catalysts has attracted tremendous interest in recent years due to their high electrocatalytic activities and stability in methanol oxidation reactions (MORs). Herein, we report an eco-friendly synthetic strategy for obtaining Pt/CeO_2 composite microspheres, which are highly active and durable catalysts for MOR. The porous CeO_2 microspheres were prepared through a hydrothermal method using the *Piper longum* fruit extract, which is an environmentally friendly solvent. The Pt nanoparticles (NPs) with an average size of ∼5 nm dispersed on CeO_2 microspheres were obtained by the chemical reduction of Pt^{2+} ions at room temperature. It was found that the supported Pt NPs are strongly coupled through strong metal−support interactions (SMSIs), which promoted the formation of oxygen vacancies (OVs) and increased the concentration of active Ce^{3+} sites. Owing to the presence of high OVs and of Ce^{3+} species, the Pt/CeO_2 microsphere catalyst revealed enhanced MOR performance, with specific activity (SA) as high as 36.37 mA/cm^2 and mass activity (MA) of 229.44 mA/mg, which are substantially higher than those of commercial catalysts such as Pt/C and Pt/CeO_2 prepared with commercial CeO_2 nanoparticles. Moreover, the resultant catalyst showed excellent durability, retaining about 76.2% of its initial current density even after 5000 potential cycles. The used green extract-mediated synthesis process can be a promising alternative to conventional methods for the rational design of highly active metal nanoparticle-supported catalysts for heterogeneous catalysts.

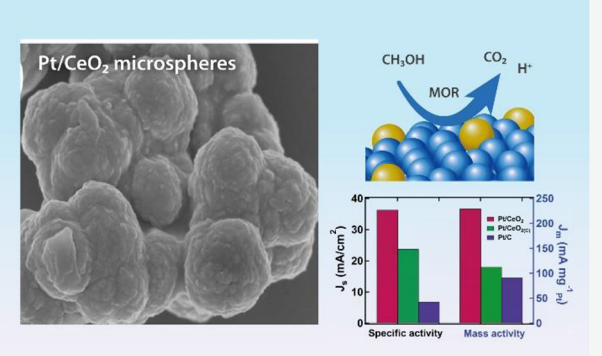

1. INTRODUCTION

Direct methanol fuel cells (DMFCs) have received tremendous interest in recent years, as they enable the development of efficient next-generation power conversion sources for transportation and portable devices.[1] DMFCs possess significant advantages such as high power density, room temperature energy conversion, and low environmental pollution over other energy sources, especially among the existing hydrogen fuel cells.[2,3] To oxidize a methanol molecule completely into water and carbon dioxide (CO_2), a reaction based on a six-electron transfer process is needed, which is hard to achieve without introducing efficient electrocatalysts.[4] Metallic Pt is one of the most efficient noble-metal catalysts, extensively exploited as a model catalyst for methanol oxidation reactions (MORs) because of its unique d-band contributed electronic structure, which facilitates the adsorption and dissociation of methanol molecules at its surface.[5,6] However, the efficiency of MOR with Pt catalysts is highly restricted by carbon monoxide (CO) poisoning during their operations as electrode materials. The surface adsorbed CO intermediates strongly bind to the Pt surface, leading to the blockage of Pt active sites for MOR. Such a loss of catalytic sites at the surface of the electrocatalysts results in a substantial reduction in their catalytic activity and durability.[7,8] On the other hand, the high cost and poor cycling durability impede their large-scale application in DMFCs.[9] Hence, designing stable electrocatalysts that are resilient to CO poisoning on the Pt surface and maximizing the MOR efficiency and operational stability are crucial for developing high-performance DMFCs.[9]

To tackle the above-mentioned challenges, substantial research efforts have been devoted to the development of alternative electrocatalysts. The most promising approaches adopted for this purpose are alloying Pt with other transition metals, such as Co, Cu, Ni, Ru, etc.,[10] and embedding the Pt

Received: July 18, 2022
Revised: October 14, 2022
Published: November 1, 2022

catalyst with metal oxide supports, such as TiO_2,[11] SnO_2,[12] SiO_2,[13] CeO_2,[14] $WO_3/W_{18}O_{49}$,[15,16] etc. While both strategies have worked well for improving the performance of catalytic electrodes, the latter strategy seems to be more advantageous considering the performance, stability, and extent of CO tolerance of the metal-oxide-supported Pt catalysts. Moreover, it reduces the consumption of Pt, which is a very costly precious metal.[17,18] Among the metal oxides, cerium dioxide (CeO_2) has been considered as an emerging material capable of supporting a wide variety of metal catalysts, with fascinating physicochemical properties, including the high capacity of oxygen storage,[19] ability to change the oxidation state of Ce between Ce^{3+} and Ce^{4+} in a reversible manner,[20] and high metal dispersion capacity.[21] Incorporation of small Pt nanoparticles (NPs) at the surface of CeO_2 support increases its oxygen storage efficiency and oxygen mobility[19] and prevents oxidation during chemical reactions.[22] Numerous research groups fabricated Pt and Pd nanoparticle supported CeO_2 catalysts for applying them in catalytic reactions of different types.[23−25] Specifically, supported Pd or Pt single atoms/clusters and their strong metal−support interaction (SMSI) are seen to substantially improve the electrocatalytic performance and stability of CeO_2 in various catalytic reactions.[26−29] From the earlier studies, it is evident that the performance of the Pt/CeO_2 catalyst critically depends on the size of Pt NPs,[30−32] their dispersion over the CeO_2 support,[32] the facets of CeO_2 crystallites,[33] and the Pt−CeO_2 interface through SMSI.[34,35] Specifically, it has been reported that the SMSI between supported Pt NPs and CeO_2 support can induce a large electronic perturbation on the supported Pt NPs and the formation of oxygen vacancies at the metal−CeO_2 interface, which are largely responsible for enhancing the MOR performance.[22,36] Therefore, engineering the interface of Pt/CeO_2 nanocomposites to achieve an SMSI through the formation of a Pt−O−Ce bond can play a pivotal role in maximizing the MOR performance of the composite electrocatalyst.[37] Furthermore, the adequate morphology and porous structural features of CeO_2 support can also facilitate the stabilization of supported Pt NPs along with an enhancement of the specific surface area, contributing to the overall catalytic performance and durability of the catalyst.[38]

In the past few years, numerous synthetic approaches have been implemented to prepare CeO_2 nanostructures and Pt/CeO_2 composites with controlled size, morphology, and pore structures.[35−39] Most of these methods involve chemical processing, where surfactants or capping agents are used for tuning the morphology, size, and porosity of CeO_2 and Pt/CeO_2 nanostructures. While a significant progress has been made on the controlled synthesis of these nanostructures, fabrication of porous metal NP-supported metal oxide nanostructures with precise control of surface area and dispersion of metal NPs over the support on a large scale remained a challenge. Therefore, the development of new synthesis protocols that are environmentally friendly and low cost received massive attention in recent years for fabricating metal-oxide-supported Pt NPs of desired characteristics to apply them as efficient catalysts in heterogeneous catalytic reactions, energy conversion, and energy storage.[39] During the past two decades, efforts have been made to utilize green and eco-friendly media such as the extracts of different plants, fruits, and leaves as alternatives to the conventional chemical solvents, which also act as reductors and surfactants for the controlled synthesis of metal, semiconductor, and composite nanostructures.[40,41] In this aspect, piperine extracts from long pepper fruit are of particular interest, which have been applied for synthesizing different nanostructured materials, including metal, metal oxide, and metal−metal oxide composites.[40,41] The polyphenol groups in piperine extracts are known to be responsible for reducing metal ions and the subsequent stabilization of the formed nanostructures.[42] Previously, we demonstrated the use of the *Piper longum* fruit extract for synthesizing uniform metal oxide nano/microstructures such as Cu_2O and NiS_2 microspheres, which showed remarkably high electrochemical performance in Li-ion batteries (LIBs).[43,44]

In the present study, we report on the synthesis of a Pt/CeO_2 composite with good dispersion of Pt NPs over CeO_2 microspheres by a two-step synthesis approach using the hydrothermal and chemical reduction process. The hydrothermal synthesis of CeO_2 microspheres was performed using the *Piper longum* fruit extract, which is a natural and environmentally friendly solvent. The chemical reduction technique was utilized to grow the Pt NPs over the prefabricated CeO_2 microspheres. The structural and morphological characteristics of the Pt/CeO_2 composite microspheres along with their composition and interfacial interactions were investigated using SEM, HR-TEM, XRD, and XPS analysis. The composite microstructures were utilized as electrocatalysts for MORs. As-prepared Pt/CeO_2 composite microspheres manifested an outstanding catalytic performance toward MOR relative to the commercial Pt/C and Pt/CeO_2 catalysts obtained using commercial CeO_2 nanoparticles (Pt/CeO_2(C)). The Pt/CeO_2 composite microspheres revealed excellent durability as electrocatalysts, retaining about 76.2% of its initial current density even after 5000 cycles.

2. EXPERIMENTAL SECTION

2.1. Chemicals. Cerium(III) nitrate hexahydrate ($Ce(NO_3)_3{\cdot}6H_2O$, 99.99%), hexachloroplatinic acid ($H_2PtCl_6{\cdot}6H_2O$, 99.99%), palladium(II) chloride ($PdCl_2$, ≥99.9%), and sodium borohydride ($NaBH_4$, ≥98%), all analytical grade, were purchased from Sigma-Aldrich, Taiwan, and utilized as received. Commercial cerium(IV) oxide nanoparticles (powder, particle size <25 nm) were also bought from Sigma-Aldrich, Taiwan. All the stock solutions and electrolyte solutions utilized for synthesis and electrochemical studies, respectively, were prepared using Milli-Q deionized (DI) water of resistivity >18.2 MΩ·cm.

2.2. Preparation of the *Piper longum* Fruit Extract. The *Piper longum* fruit extract was prepared using the matured fruits of Indian long pepper plants collected from an agricultural area in the southern part of India. The brown-colored long pepper fruits were collected and thoroughly washed several times with DI water and ethanol and dried at room temperature for a week. After that, the dried samples were grounded into fine powder in a commercial mixer grinder. To obtain the homogeneous *Piper longum* fruit extract, about 1.0 g of the obtained power was added to 100 mL of ethanol and kept under magnetic stirring for 30 min at room temperature (RT, 30 °C). Finally, the obtained mixture was filtered using 90 mm Whatman filter paper (grade 201) to separate the residue from the supernant. The solution containing the *Piper longum* fruit extract was stored at the ambient condition for utilization in the synthesis process.

2.3. Synthesis of CeO_2 Microspheres. The CeO_2 microspheres were synthesized using a simple hydrothermal

https://doi.org/10.1021/acs.jpcc.2c05069
J. Phys. Chem. C 2022, 126, 18670−18682

Scheme 1. Typical Synthetic Steps Involved in the Preparation of the Pt/CeO_2 Composite Microsphere Catalyst for Efficient MOR

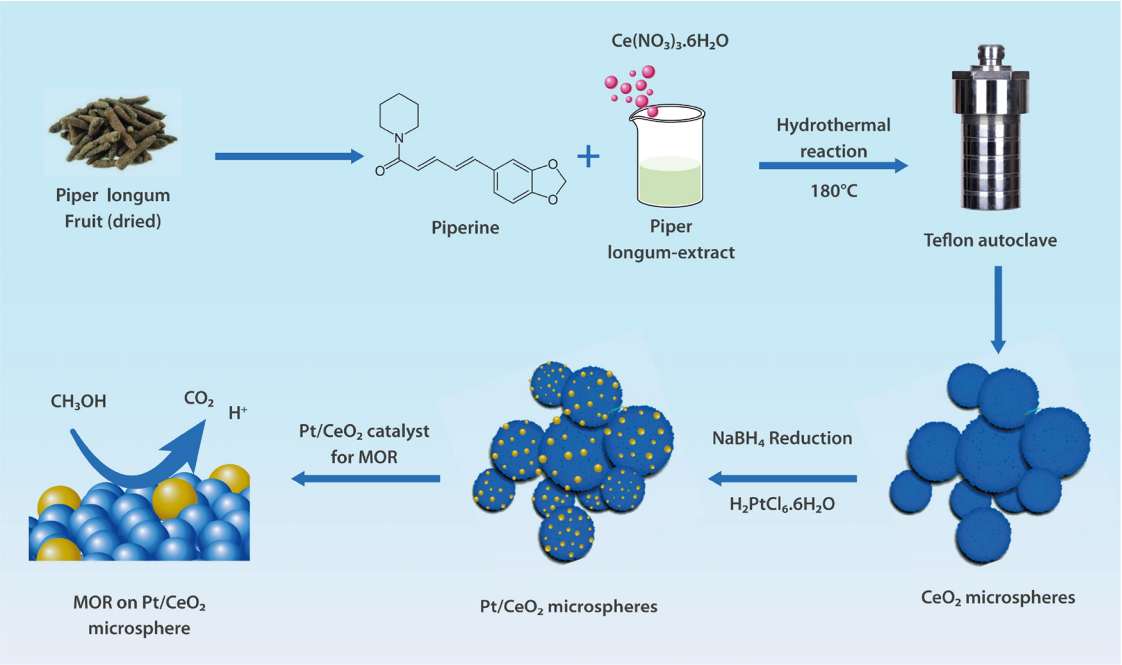

method. In a typical synthesis, 500 mg of $Ce(NO_3)_3{\cdot}6H_2O$ was added to 50 mL of a freshly prepared *Piper longum* extract solution under magnetic stirring. After about 1 h of magnetic stirring, the precursor solution was transferred to a 100 mL Teflon-lined stainless autoclave. Then, the autoclave was heated at 180 °C for 12 h in a programmable oven, increasing the temperature at 5 °C/min from the room temperature. After that, the oven was allowed to cool down to RT. The product formed in the autoclave was separated by centrifugation at 6000 rpm for 15 min and washed with DI water and ethanol four times to remove the surface-adhered organic residues and mineral nutrients such as K^+, Na^+, Mg^{2+}, etc. Finally, the sample was dried in an oven at 80 °C for 6 h and stored at room temperature.

2.4. Synthesis of Pt/CeO_2 Composite Microspheres. The Pt NPs were formed over the presynthesized CeO_2 microspheres by a simple chemical reduction process. Briefly, 50 mg of the presynthesized CeO_2 microsphere sample was dispersed in 50 mL of DI water by magnetic stirring for 30 min. Then, a freshly prepared 50 mL (0.1 M) $NaBH_4$ solution was added to it and magnetically stirred for another 30 min. Afterward, 10 mL (5 mM) of the Pt precursor ($H_2PtCl_4{\cdot}6H_2O$) solution was quickly injected to the earlier solution, and the reaction was continued for 1 h under magnetic stirring. The final products were collected by centrifugation at 600 rpm, washed four times with ethanol and DI water, and dried in an oven at 60 °C for 2 h. The Pt nanoparticle-supported commercial CeO_2 nanoparticles were prepared following a similar process, replacing only the as-synthesized CeO_2 microspheres by commercial CeO_2 NPs (particle size <25 mn) in the earlier mentioned process. The Pt/CeO_2 nanocomposite sample prepared using commercial CeO_2 NPs was designated as Pt/CeO_2(C). For comparison, Pd/CeO_2 composite microparticles were also prepared by reducing Pd ions (from a Na_2PdCl_4 precursor solution) over the as-synthesized CeO_2 microspheres utilizing the same procedure but replacing $H_2PtCl_4{\cdot}6H_2O$ with Na_2PdCl_4 in the reaction mixture.

2.5. Electrochemical Analysis. The electrochemical analysis of the as-synthesized CeO_2 microspheres and Pt/CeO_2 and Pd/CeO_2 composites microspheres was carried out in a standard three-electrode electrochemical workstation. A glassy carbon (GC) electrode modified with the synthesized electrocatalysts was used as the working electrode, a commercial Ag/AgCl electrode was used as a reference, and a platinum wire was utilized as the counter electrode. Before fabricating the working electrodes, the GC electrode surface was polished well with alumina powder (diameter ~5 nm), washed with a water−acetone (1:1) mixture, and ultrasonicated for 15 min in DI water. Then, about 10 μL of a viscous solution prepared by homogeneous mixing of Pt/CeO_2 (1 mg/mL) and liquid Nafion was drop-casted over the GC electrode and dried at room temperature. A CHI 650C (Austin, TX, USA) electrochemical workstation was utilized to conduct all the electrochemical tests. The cyclic voltammetric (CV) and chronoamperometric (CA) analyses were carried out in 1 M KOH containing 1 M CH_3OH. Before recording the CV curves, the electrolyte solution was purged with nitrogen gas for 30 min to remove the dissolved oxygen from it. The electrochemical impedance spectroscopy (EIS) measurements were carried out in 1 M KOH containing 1 M CH_3OH at a potential of −0.2 V (vs Ag/AgCl). The CO stripping voltammetry was carried out in 1 M of KOH solution. Prior to recording the CO stripping profiles, the electrolyte solution was first purged with ultrapure argon (Ar) for 30 min, and then gaseous CO (0.1% CO containing Ar gas) was bubbled for 60 min at a fixed potential of 0.0 (*vs* Ag/AgCl) for the formation of the CO adlayer onto the electrocatalyst surface. The CO stripping voltammetry profiles were recorded at a scan rate of 50 mV s^{-1}. For DMFC tests, the anode and cathode were assembled into a fuel cell, and the activity was recorded by discharging tests at 20 °C using a battery testing

https://doi.org/10.1021/acs.jpcc.2c05069
J. Phys. Chem. C 2022, 126, 18670−18682

system, following the previously described procedure.[45] The concentrations of methanol and KOH in the electrolyte were 5.0 and 4.0 M, respectively.

2.6. Material Characterization. The morphology and elemental composition of the prepared samples were analyzed in a Hitachi SU800 field emission scanning electron microscope (FE-SEM) coupled with an X-ray energy dispersive spectrometer (EDX). Transmission electron microscopic (TEM) images of the samples were obtained in a JEOL 2100F (JEOL, National Cheng Kung University, Taiwan) microscope. For TEM inspection, the samples were prepared by drop-casting the colloidal solutions of the powder samples prepared in ethanol over carbon-coated Cu grids. The crystallinity of the samples was examined in an X'Pert PRO Analytical X-ray diffractometer (PANalytical, National Cheng Kung University, Taiwan) with monochromatized Cu Kα radiation (λ = 0.15406 nm). A nonreflective Si sample holder was employed to minimize the background. Nitrogen (N_2) adsorption−desorption isotherms of the samples were acquired in a Micrometrics ASAP 2020 (National Cheng Kung University, Taiwan) sorptometer after degassing them at 180 °C for 3 h. Fourier transform infrared (FTIR) spectra of the sample were measured using an Agilent FTIR spectrometer. The composition and chemical state of the constituting elements in the samples were analyzed in an X-ray photoelectron spectrometer (PHI Quantera SXM, ULVAC-PHI, National Cheng Kung University, Taiwan) employing X-ray radiation of an Al Kα target (1.4 × 0.1 mm, 100 W, 20 kV, 5 mA). Room temperature optical absorption spectra of the samples were recorded in a Shimadzu UV-2600 spectrophotometer. The loading amount of Pt and Pd was estimated by inductively coupled plasma optical emission spectrometry (ICP-OES) using a Perkin-Elmer Optima 5300 DV ICP-OES spectrometer. The as-synthesized Pt/CeO_2 and Pd/CeO_2 composite microspheres were digested in aqua regia for 48 h to dissolve them completely and then diluted with the required amount of DI for performing ICP-OES measurements.

3. RESULTS AND DISCUSSION

3.1. Structural and Morphological Characterization of Pt/CeO_2 Composite Microspheres. The steps involved in the synthesis of Pt/CeO_2 composite microspheres are schematically illustrated in Scheme 1. The bare CeO_2 microspheres were first synthesized using a green approach based on a *Piper longum* fruit extract-mediated hydrothermal process performed at 180 °C for 12 h. In the used synthesis process, CeO_2 microspheres were formed through the hydrothermal decomposition of $Ce(NO_3)_3{\cdot}6H_2O$ precursor salts into CeO_2.[46] The *Piper longum* fruit extract contains long-chain piperine, which possesses phenolic groups,[42] as confirmed from its Fourier transform infrared (FTIR) spectrum (Figure S1, Supporting Information). The FTIR spectrum of the *Piper longum* fruit extract revealed well-defined absorption bands around 3344 and 2974 cm^{-1} corresponding to O−H stretching vibrations of the phenol group and C−H stretching vibration of aromatic compounds. The band that appeared around 1379 cm^{-1} is assigned to the O−H bond of polyphenol.[42,47] These phenolic compounds serve as capping agents during the thermal decomposition process, which enables the growth of CeO_2 microspheres.[43] The microspheres are composed of small ceria particles, which aggregate to form the microspheres, probably due to the low solubility of $Ce(NO_3)_3{\cdot}6H_2O$ in the *Piper longum* fruit extract. Such low solubility of the ceria precursor in the extract facilitates the aggregation of initially formed small ceria particles into microspheres.

To understand the role of the *Piper longum* fruit extract in the formation of CeO_2 microspheres, the synthesis was also carried out without the assistance of the fruit extract, keeping all the other experimental conditions the same (Figure S2, Supporting Information). The low- and high-magnification SEM images of these test CeO_2 NPs revealed the formation of nonuniform spherical particles instead of microspheres composed of tiny CeO_2 particles. The result indicates how the plant extract facilitates the formation of CeO_2 microspheres, serving as a stabilizing agent. The FTIR spectrum (Figure S3, Supporting Information) of the CeO_2 microsphere sample prepared using the *Piper longum* extract also revealed the presence of phenolic groups. Notably, the band at 2938 cm^{-1} related to C−H stretching was not observed in CeO_2 particles obtained without using the *Piper longum* fruit extract.

The synthesis protocol utilized in the present study showed good reproducibility, and the *Piper longum* fruit extract storage condition did not affect the morphology and crystallinity of the CeO_2 microsphere even after 1 month storage at room temperature (Figure S4a−e, Supporting Information). On the other hand, a simple chemical reduction method was adapted to decorate the presynthesized CeO_2 microspheres with small Pt NPs uniformly. The strong reducing power of $NaBH_4$ enabled the reduction of Pt^{2+} ions to form metallic (Pt^0) NPs of small sizes uniformly dispersed on CeO_2 support.[48] Notably, the aggregated CeO_2 microspheres with rough surfaces facilitate the formation of nanopores, which are beneficial for the stabilization of small Pt NPs over the microspheres. The pores present at the surface of CeO_2 could confine the Pt^{2+} ions and their subsequent reduction by the $NaBH_4$ solution, enabling the formation of ultrasmall Pt NPs with control over size and dispersity onto the CeO_2 microspheres' surface.[45,49]

The morphology of the bare CeO_2 and Pt/CeO_2 composite microsphere samples was examined using an FE-SEM. From the representative FE-SEM images of the samples presented in Figure S5a,b (Supporting Information), we can see that the pristine CeO_2 microspheres exhibit a uniform spherical morphology with a rough surface, and their sizes vary between 300 and 500 nm. It can also be noticed that the CeO_2 microspheres are composed of smaller CeO_2 particles, which serve as primary particles or building units of the CeO_2 microspheres. Figure S5c,d (Supporting Information) displays typical SEM images of the Pt/CeO_2 composite microspheres. As can be noticed, the Pt/CeO_2 composite microspheres bear similar morphology and sizes as those of the pristine CeO_2 microspheres. Although the formation of Pt NPs over the composite microspheres cannot be perceived from these SEM images, energy dispersive X-ray spectroscopy (EDS) elemental mapping images of the sample (Figure S5e, Supporting Information) clearly demonstrate a uniform distribution of Pt elements over the CeO_2 microspheres. In fact, all the elements, i.e., Ce (red), O (green), and Pt (yellow), remained homogeneously distributed over the composite microspheres, indicating the excellent dispersion of the supported Pt NPs. Additionally, the EDS spectrum of the sample (Figure S6a, Supporting Information) revealed only the emissions of Ce, O, and Pt, with no additional emission (apart from the Si emission band appearing from the substrate utilized to support the samples) associated to any other element, suggesting the high

https://doi.org/10.1021/acs.jpcc.2c05069
J. Phys. Chem. C 2022, 126, 18670−18682

purity of the synthesized samples. The amount of Pt loaded over the Pt/CeO_2 composite microspheres estimated from EDX analysis was about 16.20 wt % (table in Figure S6b, Supporting Information). Inductively coupled plasma (ICP) analysis of the sample also revealed a similar (16.60 wt %) Pt content in it (Figure S7, Supporting Information).

For a detailed analysis of the morphology and atomic-level structure of the pristine CeO_2 and Pt/CeO_2 microspheres, their low- and high-resolution TEM (HR-TEM) images were recorded. Figure 1a–c presents the representative TEM and

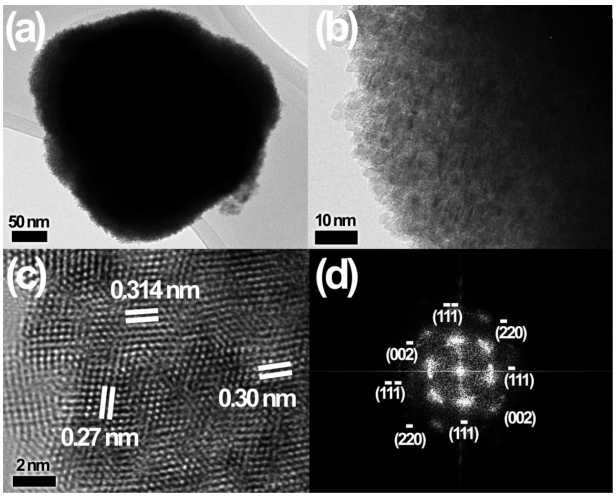

Figure 1. (a) Typical low- and (b) high-resolution TEM images of as-prepared pristine CeO_2 microspheres. (c) Typical HR-TEM image and (d) corresponding FFT pattern of a pristine CeO_2 microsphere.

HR-TEM images of the pristine CeO_2 microspheres. As can be seen in Figure 1a, the pure CeO_2 microspheres display a spherical morphology with size varying in the 300–500 nm range. A close look of the amplified TEM image of the sample (Figure 1b) revealed that the pristine CeO_2 microspheres are composed of smaller CeO_2 particles, which are assembled to form CeO_2 microspheres. The HR-TEM images of the CeO_2 microparticles (Figure 1c) revealed exposed crystal planes, with interplanar spacing (d-spacing) values of 0.27, 0.30, and 0.314 nm, which correspond to the {100} and {111} planes of CeO_2 in cubic (fluorite) phase.[45,50] The fast Fourier transform (FFT) pattern of the HR-TEM image presented in Figure 1d further confirms the similar interplanar d-spacings of the CeO_2 lattice.

To examine the successful incorporation of Pt NPs and their dispersion over the surface of CeO_2 microspheres, TEM and HR-TEM images of the Pt/CeO_2 composite microsphere sample were recorded. Figure 2a–c and Figure S8 (Supporting Information) display the TEM images of the as-prepared Pt/CeO_2 composite microspheres, which revealed that pristine CeO_2 microspheres maintain their original morphology even after the incorporation of Pt NPs. The high-magnification TEM image of a Pt/CeO_2 composite microsphere presented in Figure 2c shows the formation of small Pt NPs with an average size of 5.0 nm (inset of Figure 2c), which are distributed uniformly over the CeO_2 microsphere. The small Pt NPs formed over the CeO_2 support can be readily distinguished by their darker contrast (marked by blue circles). Figure 2d,e shows the representative HR-TEM images of Pt/CeO_2 composite microspheres demonstrating that the Pt NPs formed over them are in intimate contact. Such strong contact between the Pt NPs and the CeO_2 support can facilitate the electron transfer process between them at the interface, which is highly desirable for boosting the electrocatalytic performance of the composite structures.[51] The estimated d-spacing value of 0.272 nm corresponds to the (100) planes of CeO_2, and the lattice spacing value of 0.225 nm corresponds to the (111) plane of metallic Pt in face-centered cubic (fcc) phase (Figure 2e).[52] The FFT patterns of the selected regions of the HR-TEM image (Figure 2d) revealed similar lattice spacing values for the CeO_2 support and crystalline fcc Pt NPs grown over it. A slight lattice expansion was observed (0.272 nm) in the Pt/CeO_2 composite microspheres relative to the pristine CeO_2 microspheres (0.27 nm). This small increase in the d-spacing value for the Pt/CeO_2 microspheres might be due to the strong electronic coupling between the ultrasmall Pt NPs and the CeO_2 support surface.[53] Furthermore, the average crystallite sizes of CeO_2 in the pristine CeO_2 and Pt/CeO_2

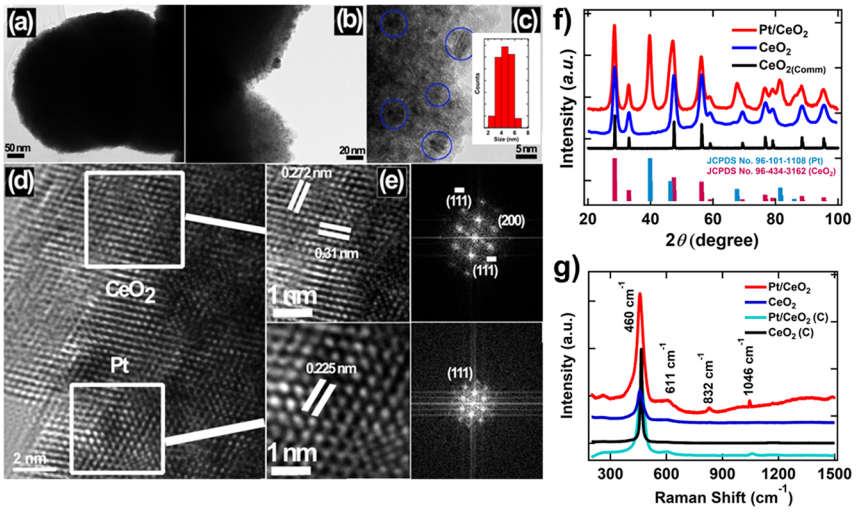

Figure 2. (a–c) Typical TEM images of Pt/CeO_2 microspheres. The inset of panel c shows the distribution histogram of Pt NPs. (d) Typical HR-TEM image of a Pt/CeO_2 microsphere and (e) magnified image of the marked sections (white square regions) of CeO_2 and Pt NPs in panel d, along with their FFT patterns. (f) X-ray diffraction (XRD) pattern. (g) Raman spectra of pure CeO_2, Pt/CeO_2 samples.

https://doi.org/10.1021/acs.jpcc.2c05069
J. Phys. Chem. C 2022, 126, 18670–18682

composite microspheres estimated from their XRD patterns using the Scherrer formula were 54.9 and 48.3 nm, respectively. On the other hand, the average crystallite size estimated for the Pt NPs formed over CeO_2 microspheres was 2.82 nm. The observed small reduction of crystallite size of CeO_2 in the composite microspheres might be the result of the reducing atmosphere utilized for growing the Pt NPs over them.

The structure and crystallinity of the pristine CeO_2 and Pt/CeO_2 microspheres were investigated through powder X-ray diffraction (XRD) analysis. Figure 2f presents the XRD spectra of the pristine CeO_2 microspheres and Pt/CeO_2 microspheres, which are compared with the commercial CeO_2 NPs (CeO_2 NPs(C)). The XRD pattern of CeO_2 NPs(C) revealed narrow and well-defined diffraction peaks at 2θ = 28.6, 33.13, 47.54, 56.39, 59.13, 69.45, 76.73, 79.10, and 95.5°, which could be readily indexed to the (111), (200), (220), (311), (222), (331), and (420) planes of the cubic fluorite structure of CeO_2 (JCPDS 96434-3162).[54] The as-synthesized pristine CeO_2 microspheres exhibited XRD peaks at the same positions as those of the commercial CeO_2 NPs. However, the diffraction bands of the pristine CeO_2 microspheres were more intense and broader in comparison with the bands revealed for the CeO_2 NPs(C) (average size of 25 nm). For Pt/CeO_2 microspheres, there appeared additional four diffraction peaks at around 2θ = 39.8, 67.6, 81.2 and 86.1°, which correspond to the metallic Pt NPs in face-centered cubic (fcc) phase (JCPDS 96101-1108).[52] It should be noted that all the diffraction peaks corresponding to CeO_2 in the Pt/CeO_2 composite microspheres are slightly displaced toward lower 2θ values in comparison to their positions in the XRD pattern of the pristine CeO_2 microspheres, which might be due to a reduction of crystallite size in the former sample, as has been noticed in their TEM results.

The interaction between Pt NPs and CeO_2 was examined using Raman spectroscopy analysis. Figure 2g presents the Raman spectra of pure CeO_2, CeO_2(C), Pt/CeO_2, and Pt/CeO_2(C) samples. The bare CeO_2 showed two distinct peaks at 460 and 610 cm^{-1}, which are attributed to the triply degenerate F_{2g} mode of the fluorite structure and defect induced (D) mode of as-obtained CeO_2, respectively, in well accordance with the earlier studies.[48] In contrast, for the commercial CeO_2, the defect mode peak was not found. In case of Pt/CeO_2, there appeared additional peaks at 832 and 1064 cm^{-1} in comparison with the pure CeO_2, which are assigned to the vibrations originating from Pt−O or Pt−O−Ce bonds, indicating a strong interaction between Pt and CeO_2*via* Pt−O−Ce linkages.[48] Notably, these peaks are very weak (less intense) in the Pt/CeO_2(C) sample, suggesting the lack of Pt−O−Ce bond formation in the latter sample.

The details of the specific surface area (SSA) and pore size of the pristine CeO_2 and Pt/CeO_2 composite microsphere samples were investigated by recording their N_2 adsorption−desorption isotherm at 77 K using the Brunauer−Emmett−Teller (BET) method (Figure 3). As can be seen in Figure 3, both the samples revealed type IV isotherms, with an obvious H2 hysteresis loop, indicating the formation of slit-shaped mesoporous structures in the samples due to the aggregation of primary CeO_2 particles in the CeO_2 microspheres.[25,55] The SSAs of the pristine CeO_2 and Pt/CeO_2 microsphere samples were estimated to be 87.5 and 83.2 m^2/g, respectively. As can be noted, the SSA value was reduced marginally, from 87.5 to 83.2 m^2/g, after incorporating Pt NPs onto CeO_2 microspheres. The slight decrease of SSA in the Pt/CeO_2 microsphere sample can be attributed to the partial blocking of pores of CeO_2 microspheres by the formed Pt NPs at their surface. The SSA values estimated for the CeO_2 and Pt/CeO_2 composite microspheres are relatively higher than those of the CeO_2 NPs(C) (38.09 m^2/g)[56] and Pt/CeO_2 composite (52.54 m^2/g) reported earlier.[48] Such high SSA values of the CeO_2 and Pt/CeO_2 composite microspheres are probably due to their nanoporous structure and the ultrasmall size of primary particles that constitute the microsphere morphology. The pore-size distributions in the CeO_2 and Pt/CeO_2 composite microsphere samples were obtained from the desorption profile of the isotherms using the Barrett−Joyner−Halenda (BJH) method as presented in the inset of Figure 3. The estimated average pore size for the samples was about 4.0 and 2.5 nm, respectively. While the smaller pore diameter in the Pt/CeO_2 microsphere sample is in good accordance with its lower SSA, the deduction of pore size might be due to a partial blocking of the pores by the formed Pt NPs at the surface of CeO_2 microspheres.

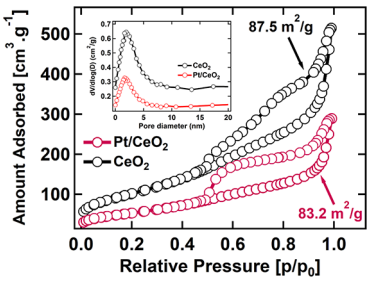

Figure 3. N_2 adsorption−desorption isotherms of pristine CeO_2 and Pt/CeO_2 microsphere samples.

To determine the composition of the sample and the chemical states of elements on their surface, the samples were analyzed by XPS. Figure 4a compares the survey spectra of CeO_2 and Pt/CeO_2 microsphere samples. As can be seen, the survey spectrum of the pristine CeO_2 sample revealed Ce and O emissions, while the Pt/CeO_2 sample revealed emissions

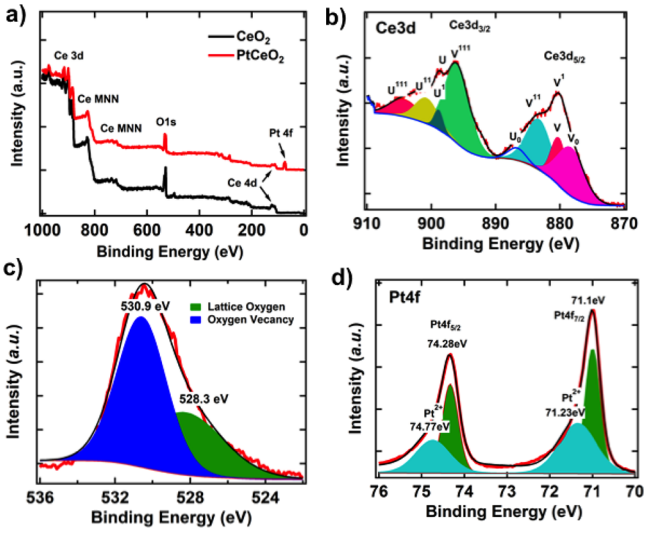

Figure 4. XPS analysis of Pt/CeO_2 composite microspheres. (a) Survey spectra of pristine CeO_2 and Pt/CeO_2 composite microspheres. Core levels of (b) Ce 3d, (c) O 1s, and (d) Pt 4f emission spectra of Pt/CeO_2 composite microspheres.

https://doi.org/10.1021/acs.jpcc.2c05069
J. Phys. Chem. C 2022, 126, 18670−18682

from Ce, O, and Pt as expected for the samples. The absence of any other emission in the spectra suggests that the samples are of high purity. To analyze the chemical state of elements in the samples, core-level spectra of Ce, O, and Pt were recorded. The deconvoluted Ce 3d emission of the pristine CeO_2 sample (Figure S9, Supporting Information) resolved five doublets, which are associated with the spin−orbit split of 3d core levels ($3d_{5/2}$ and $3d_{3/2}$) of Ce. The two doublets indicated as U^0, V^0, U, and V are related to the Ce^{3+}, and V^1, U^1, V^{11}, U^{11}, V^{111}, and U^{111} correspond to Ce^{4+}, which are in good agreement with the results reported earlier.[57,58] In the case of the Pt/CeO_2 microsphere sample, the core-level Ce 3d emission could be deconvoluted into doublets corresponding to Ce^{3+} (components at 886.8, 878.5, 899.6, and 880.4 eV) and Ce^{4+} (components at 880.2, 883.5, and 896.3 eV). As can be noticed in Figure 4b and Figure S7 (Supporting Information), the intensities of the component bands associated to the Ce^{4+} state in the Pt/CeO_2 composite are lower in comparison to their intensities in pristine CeO_2 microspheres, indicating the presence of a higher fraction of Ce^{3+} after supporting Pt NPs over the CeO_2 microspheres. From the peak area of the components, the Ce^{3+}/Ce^{4+} ratio for the Pt/CeO_2 composite sample was estimated to be about 0.76, while the same for the pristine CeO_2 sample was about 0.57 (Table S1, Supporting Information). On the other hand, compared with the pristine CeO_2, the position of the component bands in Pt/CeO_2 microsphere sample suffered a small shift toward the higher binding energy region, which could be due to a strong coupling between Pt NPs and CeO_2 support .[51] The significantly higher Ce^{3+}/Ce^{4+} ratio in the Pt/CeO_2 sample is mainly caused by the hydrogen dissociation on Pt NPs and the consumption of O atoms from the surface of pristine CeO_2 microspheres, resulting in a reduction of Ce^{4+} to Ce^{3+}.[52,56] The core-level O 1s emission of the pristine CeO_2 sample (Figure S9b, Supporting Information) could be deconvoluted into three component bands with peaks around 528.2, 532.6, and 535.0 eV, which correspond to oxygen vacancies, lattice oxygen (O_{latt}), and adsorbed oxygen (O_{ads}), respectively. However, the O 1s emission of the Pt/CeO_2 nanocomposite revealed only two components. The one peaked around 528.3 eV is associated to O_{latt}, and the other of higher intensity, which peaked around 530.9 eV, is associated to the oxygen vacancies. It should be mentioned that the intensity of the oxygen vacancy component in the core-level O 1s emission from the Pt/CeO_2 sample is comparatively higher than the same for the pristine CeO_2 sample (Figure 4c and Figure S9b), suggesting the formation of oxygen vacancies on supporting Pt NPs over CeO_2 microspheres. The increase of oxygen vacancy concentration along with the increase of Ce^{3+} concentration in the Pt/CeO_2 composite microspheres is in good accordance with the predicted formation of Pt−O−Ce linkages at their surfaces.[51] Governing such strong metal−support interaction is highly beneficial for enhancing electron transfer at the Pt−CeO_2 interface and dissolution of water (OH) molecules in the electrolyte solution to improve CO tolerance and reactivate Pt catalytic sites during MOR.[59] The high-resolution XPS spectrum of Pt 4f in the Pt/CeO_2 sample is presented in Figure 4d, which revealed its spin−orbit doublet correspond to $4f_{5/2}$ and $4f_{7/2}$ states around 74.6 and 71.8 eV binding energies, respectively.[60] The binding energy positions of both the components are at a slightly lower side than their reported positions for metallic Pt (Pt^0), indicating a possible electron transfer from the CeO_2 support to Pt NPs.[37] A deconvolution of the Pt 4f emission band revealed two doublets. While the doublet with peak positions at 74.28 and 71.10 eV corresponds to the metallic (Pt^0) state of Pt, the doublet with peaks around 74.77 and 71.23 eV corresponds to the Pt^{2+} state.[48] The presence of a small fraction of Pt^{2+} is advantageous since the Pt^{2+} ions are also found to contribute in enhancing the MOR reactivity and stability.[61]

The change of Ce^{3+} concentration after supporting Pt NPs over CeO_2 was confirmed by UV−vis analysis (Figure S10, Supporting Information). As shown in Figure S8, the bare CeO_2 microspheres exhibit an absorption peak around 324 nm, and the absorption band extends to the visible region. Such absorption in the visible range could be attributed to stable Ce^{3+} ions.[62] After incorporating Pt NPs onto CeO_2, the absorption in the visible range is slightly enhanced, which could be attributed to the increase of Ce^{3+} concentration on the surface of CeO_2. An increase in Ce^{3+} concentration leads to an occupation of the Ce 4f band and an enhancement of photon absorption in the visible region. In contrast, the Pt/CeO_2(C) sample showed a very low absorption in the visible range, suggesting a low concentration of Ce^{3+} ions in it. The UV−vis absorption results further confirm that supported Pt NPs at the CeO_2 surface can induce an increase in the Ce^{3+} concentration in the Pt/CeO_2 sample.

3.2. Electrocatalytic Performance of the Pt/CeO_2 Microspheres toward MOR. The MOR activity of the Pt/CeO_2 catalyst was evaluated, and the performance was compared with the performance of commercial Pt/C (20 wt % Pt on Vulcan carbon) and Pt/CeO_2(C) NP catalysts. The electrochemical activities and electrochemical active surface area (ECSA) of all the three catalysts were evaluated in an alkaline electrolyte solution (1 M KOH) using cyclic voltammetry (CV). Figure 5a illustrates the representative CV profiles of the Pt/CeO_2, Pt/CeO_2(C), and Pt/C catalysts recorded using N_2-saturated 1 M KOH electrolyte solution at a

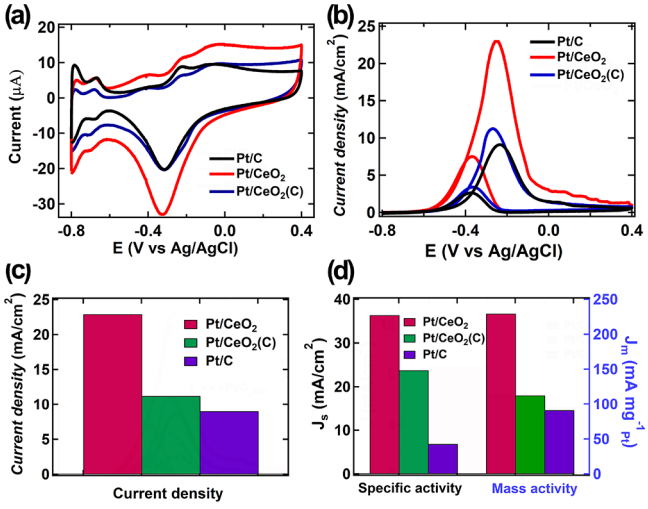

Figure 5. Electrochemical activity of the as-prepared Pt/CeO_2 microsphere catalysts for MOR. (a) CV profiles of the different catalysts in the N_2-saturated 1 M KOH solution. (b) Variation of current density with applied potential for the Pt/CeO_2, Pt/CeO_2, and Pt/C catalyst in 1 M KOH +1 M CH_3OH aqueous solution in the potential window of −0.8 to 0.4 V (*vs* Ag/AgCl) at a scan rate of 50 mV s^{-1}. (c) Corresponding bar chart diagram of current density values for each catalyst. (d) Bar chart histograms of SA and MA of the catalysts toward MOR.

https://doi.org/10.1021/acs.jpcc.2c05069
J. Phys. Chem. C 2022, 126, 18670−18682

sweep rate of 50 mV s^{-1}. In Figure 5a, we can see the appearance of distinct hydrogen adsorption/desorption regions (H_{upd}) in the potential window of −0.7 and −0.8 V, and peaks associated to the oxidation/reduction of the metal surface appeared between −0.4 and 0.4 V (*vs* Ag/AgCl) for all three studied catalysts. The Pt/CeO_2 microsphere catalyst exhibited well-defined oxidation/reduction peaks with large peak current density relative to the Pt/C and Pt/CeO_2(C) catalysts, indicating its enhanced electrocatalytic activity. The ECSA of all three catalysts was determined from the CV curves using integrated hydrogen desorption charge in the positive-going potential scan between −0.65 and −0.8 V (*vs* Ag/Ag).[63] The charge of adsorbed monolayer hydrogen on the platinum surface was assumed to be about 210 mC cm^{-2}.[60] The determined ECSA of the Pt/CeO_2 microsphere catalyst was about 6.3 m^2/g, which is smaller in comparison with the Pt/C (13.32 m^2/g) but higher than that of the Pt/CeO_2(C) catalyst (4.6 m^2/g). Additionally, ECSAs of all the catalysts were also estimated from CO-stripping measurements (Table S2, Supporting Information). The estimated ECSA value of the Pt/CeO_2 catalyst is about 44.8 m^2/g, which is slightly lower compared with the Pt/C and Pt/CeO_2(C) catalysts. The observed lower ECSA of the Pt/CeO_2 composite microsphere catalyst compared to that of Pt/C can be attributed to the slightly lower Pt NP loading onto the synthesized CeO_2 microsphere. The estimated Pt content in the Pt/CeO_2 composite microsphere using ICP was about 16.6 wt %.

The electrocatalytic MOR performance of the Pt/CeO_2 microsphere catalyst was evaluated in N_2-saturated 1 M KOH containing 1 M methanol (CH_3OH), and the results were compared with those of Pt/CeO_2(C) and Pt/C catalysts. Figure 5b displays the CV curves of the three examined catalysts in the potential range of −0.8 to 0.4 V (*vs* Ag/AgCl) with a sweep rate of 50 mV s^{-1}. The obtained CV curves were normalized to the ECSA values determined from the H_2 adsorption/desorption region in the CV profiles shown in Figure 5a. As can be noticed, all the three catalysts displayed methanol oxidation peaks during forward scans, as well as reduction peaks in reverse scans. Importantly, the Pt/CeO_2 composite microsphere catalyst registered the highest oxidation peak current density of 22.90 mA/cm^2 at a potential of −0.25 V, which is about 2.0 and 2.5 times higher than the oxidation peak current density of Pt/CeO_2(C) (11.2 mA/cm^2) and commercial Pt/C catalysts (9.0 mA/cm^2), respectively (Figure 5c). Additionally, it is evident that the oxidation potential onset of Pt/CeO_2 composite catalyst shifts more negatively toward a far lower potential of −0.52 V with respect to the oxidation potential onsets of Pt/CeO_2(C) (−0.46 V) and Pt/C (−0.41 V) catalysts, suggesting a lower activation barrier for MOR oxidation as well as higher catalytic activity of the catalyst toward MOR (Figure 5b).

Furthermore, the specific activity (SA) and mass activity (MA) of the Pt/CeO_2 composite microsphere catalyst were estimated and benchmarked against commercial Pt/C and Pt/CeO_2(C) catalysts (Figure 5d). As can see in Figure 5d, the Pt/CeO_2 catalyst has a high SA of about 36.37 mA/cm^2, which is much higher than the SA of the Pt/C (6.83 mA/cm^2) or Pt/CeO_2(C) (23.76 mA/cm^2). Moreover, the Pt/CeO_2 catalyst exhibits a much greater MA of 229.44 mA/mg_{Pt}, which is about 2.5 times higher than the MA of the commercial Pt/C (90.98 mA/mg_{Pt}) and 2.0 times higher than that of Pt/CeO_2(C) (112.33 mA/mg_{Pt}) catalysts, respectively. The results clearly demonstrate that the composite Pt/CeO_2 microsphere catalyst prepared in this study exhibits remarkably higher SA and MA values relative to the commercial catalysts such as Pt/C and Pt/CeO_2(C). The high MA could be attributed to the unique microsphere morphology of CeO_2, which stabilizes the Pt NPs on its surface with good dispersion, exposing most of them for the participation in MOR. In contrast, the Pt NPs supported onto commercial CeO_2 (Pt/CeO_2(C)) are highly agglomerated (Figure S11, Supporting Information), which could be due to the lack of a porous surface structure of commercial CeO_2 particles. These results clearly demonstrate the advantage of the porous structure of the Pt/CeO_2 microspheres prepared using the *Piper longum* fruit extract for enhancing the mass activity of the catalyst.

For a better comparison, we also synthesized two more catalysts, and their MOR performance was compared with the Pt/CeO_2 microsphere catalyst. First, Pt NPs supported onto smaller CeO_2 NPs (size of CeO_2 NPs is about 50 nm) (Figure S12, Supporting Information), and Pd NPs supported CeO_2 (Pd/CeO_2) catalyst using a chemical method without using the *Piper longum* fruit extract, keeping all other synthesis conditions the same as utilized for synthesizing the Pt/CeO_2 microsphere catalyst (Figure S13a−d, Supporting Information). The Pd loading in the obtained Pd/CeO_2 NPs was about 18.30 wt % from ICP analysis (Figure S14, Supporting Information), which is almost similar to the Pt loading in the Pt/CeO_2 microsphere sample. The Pt/CeO_2 NPs and Pd/CeO_2 catalyst showed an oxidation peak current density of 13.3 and 10 .276 mA/cm^2 against MOR, which is about 1.72 and 2.23 times lower than that of the Pt/CeO_2 microsphere catalyst (Figure S15, Supporting Information). These results unambiguously confirm that the Pt/CeO_2 microsphere catalyst exhibits considerably great MOR performance relative to the other synthesized Pt/CeO_2(C), Pt/CeO_2 NPs, and Pt/C catalysts as well as previously reported metal NPs supported catalysts as displayed in Figure 6.[64−67]

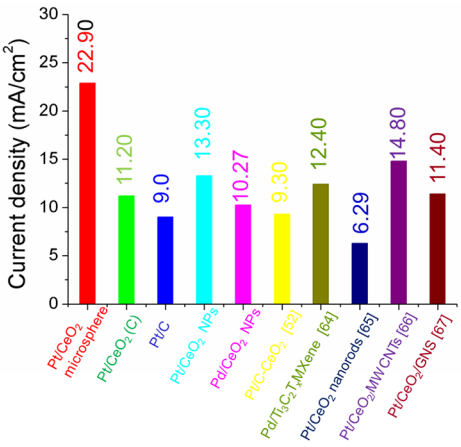

Figure 6. Comparison of the MOR performance of the Pt/CeO_2 microsphere catalyst with the other studied catalysts and some best performing Pt-supported electrocatalysts.

Electrochemical impedance spectroscopy (EIS) is considered to be an effective method to evaluate the charge transfer resistance (R_{ct}) between the electrolyte and electrode surface during MOR. Therefore, we performed the EIS spectroscopy of the fabricated electrodes to study the charge transfer efficiency of the obtained catalysts. As can be seen in Figure S16 (Supporting Information), the arc radius of the EIS

https://doi.org/10.1021/acs.jpcc.2c05069
J. Phys. Chem. C 2022, 126, 18670−18682

spectrum corresponding to the Pt/CeO_2 microsphere sample is much smaller than that of the other studied catalysts, indicating that the Pt/CeO_2 microspheres possess a high charge transfer efficiency at the electrolyte/electrode interface during MOR.

The long-term durability of an electrocatalyst is another prerequisite parameter for its practical applications in DMFCs. Therefore, the stability of the Pt/CeO_2 microsphere catalyst was assessed by conducting a chronoamperometry (CA) study over them at a fixed potential of −0.25 V (*vs* Ag/AgCl) over 120 min (Figure 7a). As shown in Figure 7a, the Pt/C catalyst

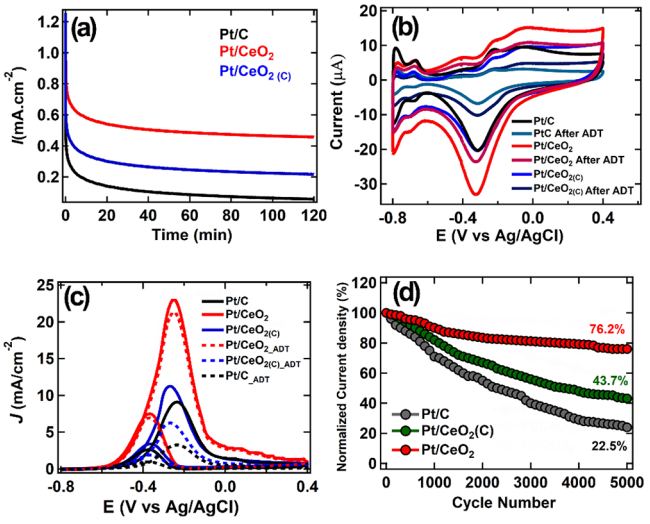

Figure 7. (a) Chronoamperometric (CA) curves of Pt/CeO_2, $Pt/CeO_2(C)$, and Pt/C catalysts recorded in 1 M KOH +1 M CH_3OH solution at the fixed potential of −0.25 V. (b) CV curves of Pt/CeO_2, $Pt/CeO_2(C)$, and Pt/C catalysts before and after ADTs. (c) Variation of current density with applied potential for the Pt/CeO_2, $Pt/CeO_2(C)$, and Pt/C catalysts before and after ADTs. (d) Changes in electro-oxidation peak current density with cycling number for the catalysts.

shows a rapid decay of current density at the beginning of the CA scan and then slowly until 120 min. Such fast decay of current density could be attributed to the quick adsorption of the carbonaceous intermediate (CO) generated during the MOR electro-oxidation process, which gets adsorbed on the surface Pt active sites, resulting in a reduction in the reactivity toward MOR. In contrast, the as-synthesized Pt/CeO_2 catalyst shows a relatively slow decay of current density initially; however, it retained the highest steady-state current density during the CA scan (120 min) among all the studied catalysts, indicating its excellent resilience to CO poisoning over the Pt NP surface. During the 120 min of the CA scan, the Pt/CeO_2 microsphere catalyst manifested only about 45% current density drop, in comparison to the current density drops of ∼65 and ∼95% that occurred for the $Pt/CeO_2(C)$ and Pt/C catalysts, respectively. The lower drop in current density for the Pt/CeO_2 microsphere catalyst indicates its high CO tolerance and long durability in methanol oxidation reactions.

The high cycling stability of the as-prepared Pt/CeO_2 microsphere catalyst was further tested by accelerated durability tests (ADTs) over 1000 continuous potential cycling. The stability was compared with the cycling stability of Pt/C and $Pt/CeO_2(C)$ catalysts. Figure 7b presents the CV curves recorded for the Pt/CeO_2, Pt/C, and $Pt/CeO_2(C)$ catalysts before and after ADT tests for 1000 cycles performed in N_2-saturated 1 M KOH +1 M CH_3OH electrolyte in the potential window of −0.8 to 0.4 V (*vs* Ag/AgCl) at a 50 mV s^{-1} sweep rate. All three samples revealed a reduction in redox peak current after 1000 ADT cycles. However, the Pt/CeO_2 microsphere catalyst revealed a lower reduction in the redox peak current compared with the reductions revealed for Pt/C and $Pt/CeO_2(C)$ catalysts. As the normalized ECSA of a catalyst is directly related to the available active sites for MOR, the ECSA values for the electrocatalysts were estimated after their ADT studies (Figure S17, Supporting Information). As can be seen in Figure S17 (Supporting Information), the normalized ECSA of the Pt/CeO_2 microsphere catalyst was reduced only by about 20% after 1000 cycles of ADT, while for the $Pt/CeO_2(C)$ and Pt/C catalysts, the reductions were about 40 and 35%, respectively. The results clearly indicate the high cycling durability of the Pt/CeO_2 microsphere catalyst toward MOR. Figure 7c compares the observed current densities of Pt/CeO_2, Pt/C, and $Pt/CeO_2(C)$ catalysts before and after ADTs, which also confirm the higher stability of the Pt/CeO_2 microsphere catalyst in comparison to the other two catalysts. The change of current density retention in the catalysts was tested for 5000 cycles. As can be noticed in the current density retention plots presented in figure 7d, the Pt/CeO_2 catalyst retained almost 76.2% of its initial current density after 5000 cycles, which is significantly higher than the current density retention of $Pt/CeO_2(C)$ (43.7%) and Pt/C (22.5%) catalysts. Finally, the possible change in morphology of the Pt/CeO_2 microsphere catalyst after the ADT test over 1000 cycles was tested using TEM (Figure S18, Supporting Information). Typical TEM images of the used Pt/CeO_2 microsphere catalyst presented in Figure S18 revealed that small Pt NPs are firmly attached to the CeO_2 support without any structural or morphological change, indicating the excellent cycling stability of the catalyst. The above results unambiguously confirm the outstanding durability of the Pt/CeO_2 microsphere catalyst toward MOR.

It is well known that the CO intermediate produced during MOR gets strongly adsorbed onto the Pt surface and poisons the active Pt sites, which deactivates the Pt catalysts.[68] Such strong CO adsorption on Pt surface is due to the electron donation from the 5σ (the highest occupied molecular orbital) orbital of CO to Pt and the subsequent back electron transfer from the Pt d-band structure to CO 2π^* molecular orbitals. Such electron donation by the orbital mixing process is quite strong; thus, CO gets adsorbed onto the Pt site, which cuts down the catalytic activity.[25] It is worth mentioning that the linearly bonded C═O gets strongly adsorbed on the Pt surface through Pt−C═O bonds up to a saturation coverage of approximately 0.68, which depends on the size and exposed facets of Pt NPs.[25] Moreover, it is known that the OH produced by dissociative adsorption of H_2O and mobility of oxygen adspecies (OH_{ads}) play a vital role in eliminating the surface adsorbed CO species and reactivating the catalytic sites at the surface of Pt.[25,69] The surface diffusion coefficient of OH adsorbed on Pt was reported to be about $5.61 \pm 0.84 \times 10^{-10}$ cm^2/s.[69] This CO desorption and reactivation process can be described by eq 1:

$$Pt - CO + H_2O \rightarrow Pt + CO_2 + 2H^+ + 2e^- \quad (1)$$

To understand the CO related antipoisoning ability of the Pt/CeO_2 catalyst, CO-stripping measurements were conducted, and the performance was compared with the

https://doi.org/10.1021/acs.jpcc.2c05069
J. Phys. Chem. C 2022, 126, 18670−18682

performance of the standard commercial catalysts Pt/C and $Pt/CeO_2(C)$ (Figure 8). As can be noticed in Figure 8a, in the

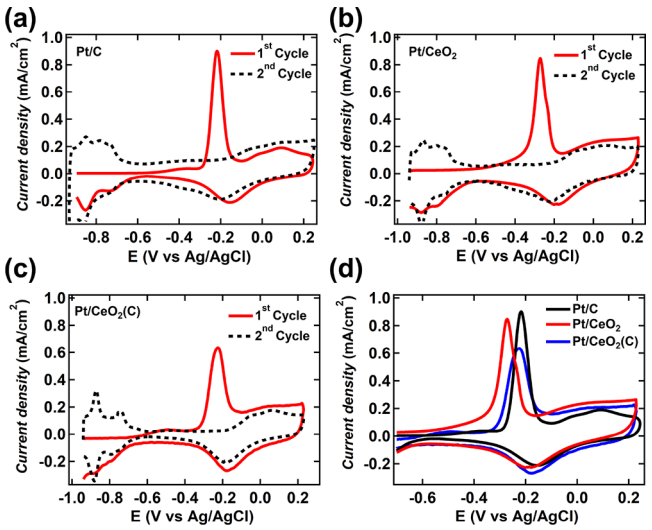

Figure 8. CO stripping profiles of (a) Pt/C, (b) Pt/CeO_2, and (c) $Pt/CeO_2(C)$ and (d) comparison of Pt/C, Pt/CeO_2, and $Pt/CeO_2(C)$ catalysts. The profiles were recorded in 1 M KOH electrolyte with a scan rate of 50 mV s^{-1}.

first anodic scan, the standard Pt/C catalysts showed a peak at −0.217 V, which can be attributed to the electro-oxidative of CO adsorption from Pt NPs.[63] However, during the second cycle, the oxidation peak disappeared, indicating an effective oxidation and removal of CO from the surface of Pt. The onset of the CO oxidation peak potential for the Pt/CeO_2 microsphere catalyst exhibited at −0.269 eV (Figure 8b) and $Pt/CeO_2(C)$ catalysts at −0.225 eV (Figure 8c). Interestingly, the onset of the CO oxidation peak potential for Pt/CeO_2 microsphere catalyst is shifted toward more negative values compared with the $Pt/CeO_2(C)$ and Pt/C catalysts (Figure 8d). Notably, the shift in the onset potential could be due to various parameters, such as the size of the Pt NPs, morphology of the CeO_2 support, and interaction between Pt NPs and CeO_2 support. The average sizes of the Pt NPs in all the prepared catalysts were almost the same. Thus, such a large shift toward more negative potential values of the CO oxidation peak for the Pt/CeO_2 microsphere catalyst could be ascribed to the generation of more OH_{ads} species, which has a lower onset potential and weakens CO adsorption on Pt sites.[25,48] Hence, the observed shift of oxidation potential toward a more negative potential suggests an impressive CO antipoisoning capability of the Pt/CeO_2 microsphere catalyst.

The possible mechanism involved in the MOR over the Pt/CeO_2 microsphere catalyst is presented in Scheme 2. The steps involved in the process are as follow: (i) the initial adsorption of MOR intermediates (CH_3OH) and OH^+ molecules at the surface of the supported Pt NPs over the CeO_2 support; (ii) the reaction of CH_3OH and OH^+, which generates the CO intermediates that strongly adsorb on Pt sites; and (iii) dissociative adsorption of OH formed from H_2O, which eliminates the adsorbed CO species on Pt sites and reactivates the Pt catalytic sites for the oxidation of CH_3O and formation of H^+ and CO_2. The synthesized Pt/CeO_2 composite microspheres act as bifunctional catalysts, where the bifunctional mechanism of oxidative CO desorption and subsequent

Scheme 2. Schematic Illustration of the Proposed Mechanism of Surface Catalytic Reaction toward Methanol Oxidation on the Pt/CeO_2 Catalyst Surface

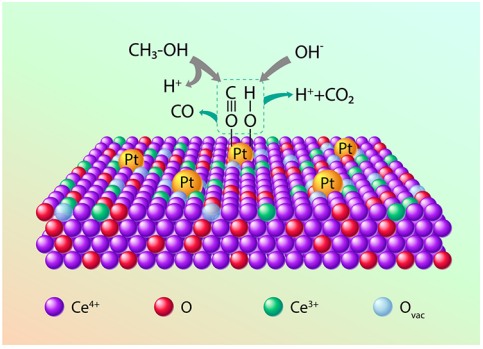

reactivation process can be described by the following relations:[4]

$$CeO_2 + H_2O \rightarrow CeO_2 - OH_{ads} + H^+ + e^- \quad (2)$$

$$Pt - CO_{ads} + CeO_2 - OH_{ads} \rightarrow Pt - CeO_2 + CO_2 + H^+ + e^- \quad (3)$$

(or)

$$Pt - CeO_2 + xCO_{ads} \rightarrow Pt + CeO_{2-x} + CO_2 \quad (4)$$

Notably, for the $Pt/CeO_2(C)$ catalyst, the onset potential was shifted toward a more negative value (−0.225 eV) relative to the Pt/C catalyst (−0.217 eV). The observed very low shift of onset oxidation potential in the $Pt/CeO_2(C)$ catalyst could be possibly attributed to the poor dispersion of supported Pt NPs and weaker coupling of the supported Pt NPs with the commercial CeO_2 NP support (Figure S11, Supporting Information) compared to that with as-prepared Pt/CeO_2 microsphere catalyst. The enhanced CO tolerance of the Pt/CeO_2 composite microsphere catalyst fabricated in this work can be attributed to the strong coupling between the supported Pt NPs and CeO_2 microsphere support through the formation of Pt−O−Ce bonds at their interfaces, which induces an electron-deficient state in the supported Pt NPs.[70] The electron-deficient Pt NPs onto the CeO_2 surface can decrease the adsorption of CO over Pt NPs due to the transfer back of electrons from the Pt 5d orbital to the empty 2π orbital of CO.[71] On the other hand, due to the strong electronegative nature of O in OH, the OH moieties bind strongly with the electron-deficient Pt species, enhancing the OH adsorption capacity of the catalyst. As a result, the CO adsorption over the Pt NP surface weakens, and the CO-resistance capacity of the Pt/CeO_2 catalyst is enhanced.

The electrochemical results presented above provide conclusive evidences of the high MOR activity and extended cycling durability of the Pt/CeO_2 microsphere catalyst, which are much superior to the MOR activity and cycling stabilities of commercial catalysts Pt/C and $Pt/CeO_2(C)$. On the other hand, Raman and XPS analysis of the composite microsphere catalyst revealed a strong interaction between the supported Pt NPs and the CeO_2 support through Pt−O−Ce linkages, increasing Ce^{3+} species at the catalyst surface. The enhanced Ce^{3+} concentration also increases the oxygen vacancies at the CeO_2 surface, improving the charge transfer process at the platinum−ceria interface. On the other hand, the CO-stripping experiments confirmed a higher negative shift of the CO-

https://doi.org/10.1021/acs.jpcc.2c05069
J. Phys. Chem. C 2022, 126, 18670−18682

oxidation peak potential for the Pt/CeO_2 composite catalyst due to the strong coupling between Pt NPs and CeO_2 support, which improves its CO poisoning tolerance. Based on the theoretical predictions reported in the literature, the intimate contact of Pt NPs with the support matrix can induce electron deficiency in the supported Pt, thus weakening CO adsorption and strengthening OH bonding at the active Pt sites.[70] Therefore, the improved MOR performance of the Pt/CeO_2 microsphere catalyst developed in this study can be attributed to the strong coupling between the Pt NPs with CeO_2 support, which also leads to a higher OH adsorption and CO desorption at the Pt surface, improving the CO poisoning and long-term durability of the catalyst.

Finally, to evaluate the performance of the anode fabricated using the Pt/CeO_2 microsphere catalyst in DMFC, we designed the polymer fiber membrane (PFM) based electrode assembly, and the polarization curves were recorded as shown in Figure S19 (Supporting Information). As can be seen, the fuel cell fabricated with the Pt/CeO_2 microsphere anode showed an open-circuit voltage of 0.90 V and generated current densities of 43.90 $mA{\cdot}cm^{-2}$ at 0.63 V and 117.26 $mA{\cdot}cm^{-2}$ at 0.15 V, respectively. The performance of the Pt/CeO_2 anode is much superior to the performance of Pd/CeO_2 catalysts reported earlier,[45] indicating the our Pt/CeO_2 microsphere catalyst prepared using the *Piper longum* fruit extract is very promising for fabricating efficient alkaline DMFCs.

4. CONCLUSIONS

In summary, we demonstrated a simple eco-friendly synthetic approach for fabricating Pt/CeO_2 composite microspheres through the *Piper longum* fruit extract mediated hydrothermal route followed by the chemical reduction of Pt^{2+} ions. The HR-TEM analysis of the composite microstructures confirmed the formation of small Pt NPs of about 5.0 nm average size over the porous CeO_2 microspheres. The Raman, XPS, and CO-stripping analyses indicated a strong interaction between the Pt NPs and the CeO_2 support at their interface through the formation of Pt−O−Ce bonds. The formation of the Pt−O−Ce bond at the interface enhances the oxygen vacancies and increases the concentration of Ce^{3+} ions at the surface of the catalyst, which improves the dissociative adsorption of OH ions, thereby limiting CO contamination onto the surface of Pt NPs. Importantly, the Pt/CeO_2 microsphere catalyst achieves a high current density and mass activity for the MOR in comparison with the state-of-art Pt/C and Pt/CeO_2(C) catalysts. In addition, the catalyst was highly resilient to CO poisoning and had excellent cycling durability, retaining about 76.2% of its initial current density even after 5000 ADT cycles. The simple, green synthesis strategy utilized to prepare the porous Pt/CeO_2 microspheres with enhanced MOR performance and high durability may pave the way for designing highly active and stable electrocatalysts for their application in DMFCs.

■ ASSOCIATED CONTENT

Supporting Information

The Supporting Information is available free of charge at https://pubs.acs.org/doi/10.1021/acs.jpcc.2c05069.

SEM images of CeO_2 obtained without fruit extract, SEM images of Pt/CeO_2, EDX elemental analysis, ICP analysis, TEM images of Pt/CeO_2, XPS spectra of CeO_2 microspheres, SEM and XRD spectrum of the Pd/CeO_2 catalyst, CV curves of the Pd/CeO_2 catalyst in MOR, ECSA details before and after ADT tests, table consisting of the concentration of Ce^{4+} and Ce^{3+} species (PDF)

■ AUTHOR INFORMATION

Corresponding Author

Siva Kumar Krishnan − *CONACYT-Instituto de Física, Benemérita Universidad Autónoma de Puebla, Puebla 72570, Mexico;* orcid.org/0000-0002-9672-9335; Email: Sivakumar@ifuap.buap.mx

Authors

Paskalis Sahaya Murpin Kumar − *Department of Civil and Environmental Engineering, Yonsei University, Seoul 03722, Republic of Korea; Research Centre for Environmental Medicine, Kaohsiung Medical University, Kaohsiung City 80708, Taiwan;* orcid.org/0000-0002-2688-1825

Subramanian Arulmani − *Research Centre for Environmental Medicine, Kaohsiung Medical University, Kaohsiung City 80708, Taiwan; Department of Chemistry, Bannari Amman Institute of Technology, Sathyamangalam, Tamil Nadu 638 401, India;* orcid.org/0000-0003-0682-9197

Hyoung-il Kim − *Department of Civil and Environmental Engineering, Yonsei University, Seoul 03722, Republic of Korea;* orcid.org/0000-0003-4358-1442

Deepthi Koolath Ramakrishnan − *Crystal Growth Centre, Anna University, Chennai, Tamil Nadu 600-025, India*

Vinoth Kumar Ponnusamy − *Research Centre for Environmental Medicine, Kaohsiung Medical University, Kaohsiung City 80708, Taiwan;* orcid.org/0000-0003-2112-2085

Umapada Pal − *Instituto de Física, Benemérita Universidad Autónoma de Puebla, Puebla 72570, Mexico;* orcid.org/0000-0002-5665-106X

Complete contact information is available at: https://pubs.acs.org/10.1021/acs.jpcc.2c05069

Notes

The authors declare no competing financial interest.

■ ACKNOWLEDGMENTS

This work was supported (in part) by the Yonsei University Research Fund (Yonsei Frontier Lab. Young Researcher Supporting Program) of 2022. S.K.K. acknowledges CONACyT, Mexico, for the Programa Investigadoras e Investigadores por México del CONACYT project (Project No. 649). U.P. thanks CONACyT, Mexico, for its help extended through grant CB 2017-2018/A1-S-26720.

■ REFERENCES

(1) Kamarudin, S. K.; Achmad, F.; Daud, W. R. W. Overview on the Application of Direct Methanol Fuel Cell (DMFC) for Portable Electronic Devices. *Int. J. Hydrogen Energy* **2009**, *34*, 6902−6916.

(2) Aricò, A. S.; Srinivasan, S.; Antonucci, V. DMFCs: From Fundamental Aspects to Technology Development. *Fuel Cells* **2001**, *1*, 133−161.

(3) Zhao, X.; Yin, M.; Ma, L.; Liang, L.; Liu, C.; Liao, J.; Lu, T.; Xing, W. Recent Advances in Catalysts for Direct Methanol Fuel Cells. *Energy Environ. Sci.* **2011**, *4*, 2736.

(4) Chung, D. Y.; Lee, K. J.; Sung, Y. E. Methanol Electro-Oxidation on the Pt Surface: Revisiting the Cyclic Voltammetry Interpretation. *J. Phys. Chem. C* **2016**, *120*, 9028−9035.
(5) Rhen, F. M. F.; McKeown, C. Enhanced Methanol Oxidation on Strained Pt Films. *J. Phys. Chem. C* **2017**, *121*, 2556−2562.
(6) Greeley, J.; Mavrikakis, M. A First-Principles Study of Methanol Decomposition on Pt(111). *J. Am. Chem. Soc.* **2002**, *124*, 7193−7201.
(7) Banham, D.; Ye, S. Current Status and Future Development of Catalyst Materials and Catalyst Layers for Proton Exchange Membrane Fuel Cells: An Industrial Perspective. *ACS Energy Lett.* **2017**, *2*, 629−638.
(8) Liu, H.; Song, C.; Zhang, L.; Zhang, J.; Wang, H.; Wilkinson, D. P. A Review of Anode Catalysis in the Direct Methanol Fuel Cell. *J. Power Sources* **2006**, *155*, 95−110.
(9) Tong, Y.; Yan, X.; Liang, J.; Dou, S. X. Metal-Based Electrocatalysts for Methanol Electro-Oxidation: Progress, Opportunities, and Challenges. *Small* **2021**, *17*, 1904126.
(10) Greeley, J.; Stephens, I. E. L.; Bondarenko, A. S.; Johansson, T. P.; Hansen, H. A.; Jaramillo, T. F.; Rossmeisl, J.; Chorkendorff, I.; Nørskov, J. K. Alloys of Platinum and Early Transition Metals as Oxygen Reduction Electrocatalysts. *Nat. Chem.* **2009**, *1*, 552−556.
(11) Antolini, E. Photo-Assisted Methanol Oxidation on Pt-TiO_2 Catalysts for Direct Methanol Fuel Cells: A Short Review. *Appl. Catal., B* **2018**, *237*, 491−503.
(12) Liu, M.; Tang, W.; Xie, Z.; Yu, H.; Yin, H.; Xu, Y.; Zhao, S.; Zhou, S. Design of Highly Efficient Pt-SnO_2 Hydrogenation Nanocatalysts Using Pt@Sn Core-Shell Nanoparticles. *ACS Catal.* **2017**, *7*, 1583−1591.
(13) Melvin, A. A.; Joshi, V. S.; Poudyal, D. C.; Khushalani, D.; Haram, S. K. Electrocatalyst on Insulating Support? Hollow Silica Spheres Loaded with Pt Nanoparticles for Methanol Oxidation. *ACS Appl. Mater. Interfaces* **2015**, *7*, 6590−6595.
(14) Chang, K.; Zhang, H.; Cheng, M. J.; Lu, Q. Application of Ceria in CO_2 Conversion Catalysis. *ACS Catal.* **2020**, *10*, 613−631.
(15) Li, X.; Guo, S.; Hu, X.; Li, D.; Liu, Z.; Yao, W.; Zhou, Y. Bifunctional N-Doped Tungsten Trioxide Microspheres as Electrode Materials for Lithium-Ion Batteries and Direct Methanol Fuel Cells. *J. Phys. Chem. C* **2020**, *124*, 21261−21267.
(16) Lu, Y.; Jiang, Y.; Gao, X.; Wang, X.; Chen, W. Strongly Coupled Pd Nanotetrahedron/Tungsten Oxide Nanosheet Hybrids with Enhanced Catalytic Activity and Stability as Oxygen Reduction Electrocatalysts. *J. Am. Chem. Soc.* **2014**, *136*, 11687−11697.
(17) Yu, W.; Porosoff, M. D.; Chen, J. G. Review of Pt-Based Bimetallic Catalysis: From Model Surfaces to Supported Catalysts. *Chem. Rev.* **2012**, *112*, 5780−5817.
(18) Esposito, D. V.; Chen, J. G. Monolayer Platinum Supported on Tungsten Carbides as Low-Cost Electrocatalysts: Opportunities and Limitations. *Energy Environ. Sci.* **2011**, *4*, 3900−3912.
(19) Mullins, D. R. The Surface Chemistry of Cerium Oxide. *Surf. Sci. Rep.* **2015**, *70*, 42−85.
(20) Montini, T.; Melchionna, M.; Monai, M.; Fornasiero, P. Fundamentals and Catalytic Applications of CeO_2-Based Materials. *Chem. Rev.* **2016**, *116*, 5987−6041.
(21) Bruix, A.; Lykhach, Y.; Matolínová, I.; Neitzel, A.; Skála, T.; Tsud, N.; Vorokhta, M.; Stetsovych, V.; Ševčíková, K.; Mysliveček, J.; et al. Maximum Noble-Metal Efficiency in Catalytic Materials: Atomically Dispersed Surface Platinum. *Angew. Chem., Int. Ed.* **2014**, *53*, 10525−10530.
(22) Reina, T. R.; Gonzalez-Castaño, M.; Lopez-Flores, V.; Martínez T, L. M.; Zitolo, A.; Ivanova, S.; Xu, W.; Centeno, M. A.; Rodriguez, J. A.; Odriozola, J. A. Au and Pt Remain Unoxidized on a CeO_2-Based Catalyst during the Water-Gas Shift Reaction. *J. Am. Chem. Soc.* **2022**, *144*, 446−453.
(23) Tran, N. D.; Farnesi Camellone, M.; Fabris, S. Probing the Reactivity of Pt/Ceria Nanocatalysts toward Methanol Oxidation: From Ionic Single-Atom Sites to Metallic Nanoparticles. *J. Phys. Chem. C* **2018**, *122*, 17917−17927.
(24) Xu, H.; Wang, A.-L.; Tong, Y.-X.; Li, G.-R. Enhanced Catalytic Activity and Stability of Pt/CeO_2 /PANI Hybrid Hollow Nanorod Arrays for Methanol Electro-Oxidation. *ACS Catal.* **2016**, *6*, 5198−5206.
(25) Meher, S. K.; Rao, G. R. Polymer-Assisted Hydrothermal Synthesis of Highly Reducible Shuttle-Shaped CeO_2: Microstructural Effect on Promoting Pt/C for Methanol Electrooxidation. *ACS Catal.* **2012**, *2*, 2795−2809.
(26) Gao, X.; Yu, G.; Zheng, L.; Zhang, C.; Li, H.; Wang, T.; An, P.; Liu, M.; Qiu, X.; Chen, W.; Chen, W. Strong Electron Coupling from the Sub-Nanometer Pd Clusters Confined in Porous Ceria Nanorods for Highly Efficient Electrochemical Hydrogen Evolution Reaction. *ACS Appl. Energy Mater.* **2019**, *2*, 966−973.
(27) Maurer, F.; Jelic, J.; Wang, J.; Gänzler, A.; Dolcet, P.; Wöll, C.; Wang, Y.; Studt, F.; Casapu, M.; Grunwaldt, J. D. Tracking the Formation, Fate and Consequence for Catalytic Activity of Pt Single Sites on CeO_2. *Nat. Catal.* **2020**, *3*, 824−833.
(28) Du, C.; Gao, X.; Cheng, C.; Zhuang, Z.; Li, X.; Chen, W. Metal Organic Framework for the Fabrication of Mutually Interacted Pt−CeO_2−C Ternary Nanostructure: Advanced Electrocatalyst for Oxygen Reduction Reaction. *Electrochim. Acta* **2018**, *266*, 348−356.
(29) van Deelen, T. W.; Hernández Mejía, C.; de Jong, K. P. Control of Metal-Support Interactions in Heterogeneous Catalysts to Enhance Activity and Selectivity. *Nat. Catal.* **2019**, *2*, 955−970.
(30) Gänzler, A. M.; Casapu, M.; Maurer, F.; Störmer, H.; Gerthsen, D.; Ferré, G.; Vernoux, P.; Bornmann, B.; Frahm, R.; Murzin, V.; et al. Tuning the Pt/CeO_2 Interface by in Situ Variation of the Pt Particle Size. *ACS Catal.* **2018**, *88*, 4800−4811.
(31) Gänzler, A. M.; Casapu, M.; Vernoux, P.; Loridant, S.; Cadete Santos Aires, F. J.; Epicier, T.; Betz, B.; Hoyer, R.; Grunwaldt, J. D. Tuning the Structure of Platinum Particles on Ceria In Situ for Enhancing the Catalytic Performance of Exhaust Gas Catalysts. *Angew. Chem., Int. Ed.* **2017**, *56*, 13078−13082.
(32) Resasco, J.; Derita, L.; Dai, S.; Chada, J. P.; Xu, M.; Yan, X.; Finzel, J.; Hanukovich, S.; Hoffman, A. S.; Graham, G. W.; et al. Uniformity Is Key in Defining Structure-Function Relationships for Atomically Dispersed Metal Catalysts: The Case of Pt/CeO_2. *J. Am. Chem. Soc.* **2020**, *142*, 169−184.
(33) Chen, W.; Xue, J.; Bao, Y.; Feng, L. Surface Engineering of Nano-Ceria Facet Dependent Coupling Effect on Pt Nanocrystals for Electro-Catalysis of Methanol Oxidation Reaction. *Chem. Eng. J.* **2020**, *381*, No. 122752.
(34) Ou, D. R.; Mori, T.; Togasaki, H.; Takahashi, M.; Ye, F.; Drennan, J. Microstructural and Metal-Support Interactions of the Pt-CeO_2/C Catalysts for Direct Methanol Fuel Cell Application. *Langmuir* **2011**, *27*, 3859−3866.
(35) Yoon, S.; Oh, K.; Liu, F.; Seo, J. H.; Somorjai, G. A.; Lee, J. H.; An, K. Specific Metal−Support Interactions between Nanoparticle Layers for Catalysts with Enhanced Methanol Oxidation Activity. *ACS Catal.* **2018**, *8*, 5391−5398.
(36) Bruix, A.; Rodriguez, J. A.; Ramírez, P. J.; Senanayake, S. D.; Evans, J.; Park, J. B.; Stacchiola, D.; Liu, P.; Hrbek, J.; Illas, F. A New Type of Strong Metal-Support Interaction and the Production of H_2 through the Transformation of Water on Pt/CeO_2(111) and Pt/CeO x/TiO_2(110) Catalysts. *J. Am. Chem. Soc.* **2012**, *134*, 8968−8974.
(37) Tao, L.; Shi, Y.; Huang, Y. C.; Chen, R.; Zhang, Y.; Huo, J.; Zou, Y.; Yu, G.; Luo, J.; Dong, C. L.; Wang, S. Interface Engineering of Pt and CeO_2 Nanorods with Unique Interaction for Methanol Oxidation. *Nano Energy* **2018**, *53*, 604−612.
(38) An, K.; Alayoglu, S.; Musselwhite, N.; Plamthottam, S.; Lindeman, A. E.; Somorjai, G. A. Enhanced CO Oxidation Rates at the Interface of Mesoporous Oxides and Pt Nanoparticles. *J. Am. Chem. Soc.* **2013**, *135*, 16689−16696.
(39) Clarke, C. J.; Tu, W. C.; Levers, O.; Bröhl, A.; Hallett, J. P. Green and Sustainable Solvents in Chemical Processes. *Chem. Rev.* **2018**, *118*, 747−800.
(40) Nasrollahzadeh, M.; Mohammad Sajadi, S.; Maham, M.; Ehsani, A. Facile and Surfactant-Free Synthesis of Pd Nanoparticles by the Extract of the Fruits of Piper Longum and Their Catalytic Performance for the Sonogashira Coupling Reaction in Water under Ligand- and Copper-Free Conditions. *RSC Adv.* **2015**, *5*, 2562−2567.

https://doi.org/10.1021/acs.jpcc.2c05069
J. Phys. Chem. C 2022, 126, 18670−18682

(41) Tammina, S. K.; Mandal, B. K.; Ranjan, S.; Dasgupta, N. Cytotoxicity Study of Piper Nigrum Seed Mediated Synthesized SnO2 Nanoparticles towards Colorectal (HCT116) and Lung Cancer (A549) Cell Lines. *J. Photochem. Photobiol., B* **2017**, *166*, 158−168.
(42) Nakkala, J. R.; Mata, R.; Sadras, S. R. The Antioxidant and Catalytic Activities of Green Synthesized Gold Nanoparticles from Piper Longum Fruit Extract. *Process Saf. Environ. Prot.* **2016**, *100*, 288−294.
(43) Murphin Kumar, P. S.; Al-Muhtaseb, A. H.; Kumar, G.; Vinu, A.; Cha, W.; Villanueva Cab, J.; Pal, U.; Krishnan, S. K. Piper Longum Extract-Mediated Green Synthesis of Porous Cu_2O:Mo Microspheres and Their Superior Performance as Active Anode Material in Lithium-Ion Batteries. *ACS Sustainable Chem. Eng.* **2020**, *8*, 14557−14567.
(44) Murphin Kumar, P. S.; Ponnusamy, V.; Kim, H.; Hernández-Landaverde, M. A.; Krishnan, S. K.; Pal, U. Molybdenum-Doped Nickel Disulfide (NiS_2:Mo) Microspheres as an Active Anode Material for High-Performance Durable Lithium-Ion Batteries. *ACS Appl. Energy Mater.* **2022**, *5*, 6734−6745.
(45) Tan, Q.; Shu, C.; Abbott, J.; Zhao, Q.; Liu, L.; Qu, T.; Chen, Y.; Zhu, H.; Liu, Y.; Wu, G. Highly Dispersed Pd-CeO_2 Nanoparticles Supported on N-Doped Core-Shell Structured Mesoporous Carbon for Methanol Oxidation in Alkaline Media. *ACS Catal.* **2019**, *9*, 6362−6371.
(46) Vasilchenko, D.; Asanova, T.; Kolesov, B.; Tsygankova, A.; Stadnichenko, A.; Slavinskaya, E.; Gerasimov, E.; Lomachenko, K.; Boronin, A.; Korenev, S. Cerium(III) Nitrate Derived CeO_2 Support Stabilising PtOx Active Species for Room Temperature CO Oxidation. *ChemCatChem* **2020**, *12*, 1413−1428.
(47) Reddy, N. J.; Nagoor Vali, D.; Rani, M.; Rani, S. S. Evaluation of Antioxidant, Antibacterial and Cytotoxic Effects of Green Synthesized Silver Nanoparticles by Piper Longum Fruit. *Mater. Sci. Eng., C* **2014**, *34*, 115−122.
(48) Murphin Kumar, P. S.; Thiripuranthagan, S.; Imai, T.; Kumar, G.; Pugazhendhi, A.; Vijayan, S. R.; Esparza, R.; Abe, H.; Krishnan, S. K. Pt Nanoparticles Supported on Mesoporous CeO_2 Nanostructures Obtained through Green Approach for Efficient Catalytic Performance toward Ethanol Electro-Oxidation. *ACS Sustainable Chem. Eng.* **2017**, *5*, 11290−11299.
(49) Gu, D. M.; Chu, Y. Y.; Wang, Z. B.; Jiang, Z. Z.; Yin, G. P.; Liu, Y. Methanol Oxidation on Pt/CeO_2-C Electrocatalyst Prepared by Microwave-Assisted Ethylene Glycol Process. *Appl. Catal., B* **2011**, *102*, 9−18.
(50) Sharma, S. K.; Paul, B.; Pal, R. S.; Bhanja, P.; Banerjee, A.; Samanta, C.; Bal, R. Influence of Indium as a Promoter on the Stability and Selectivity of the Nanocrystalline Cu/CeO_2 Catalyst for CO_2 Hydrogenation to Methanol. *ACS Appl. Mater. Interfaces* **2021**, *13*, 28201−28213.
(51) Zhou, Y.; Liu, D.; Liu, Z.; Feng, L.; Yang, J. Interfacial Pd-O-Ce Linkage Enhancement Boosting Formic Acid Electrooxidation. *ACS Appl. Mater. Interfaces* **2020**, *12*, 47065−47075.
(52) Chu, Y. Y.; Wang, Z. B.; Jiang, Z. Z.; Gu, D. M.; Yin, G. P. A Novel Structural Design of a Pt/C-CeO_2 Catalyst with Improved Performance for Methanol Electro-Oxidation by β-Cyclodextrin Carbonization. *Adv. Mater.* **2011**, *23*, 3100−3104.
(53) Murphin Kumar, P. S.; Ponnusamy, V. K.; Deepthi, K. R.; Kumar, G.; Pugazhendhi, A.; Abe, H.; Thiripuranthagan, S.; Pal, U.; Krishnan, S. K. Controlled Synthesis of Pt Nanoparticle Supported TiO_2 Nanorods as Efficient and Stable Electrocatalysts for the Oxygen Reduction Reaction. *J. Mater. Chem. A* **2018**, *6*, 23435−23444.
(54) Sarkar, B.; Pendem, C.; Konathala, L. N. S.; Sasaki, T.; Bal, R. Pt Nanoparticle Supported on Nanocrystalline CeO_2: Highly Selective Catalyst for Upgradation of Phenolic Derivatives Present in Bio-Oil. *J. Mater. Chem. A* **2014**, *2*, 18398−18404.
(55) Lee, D.-W.; Jin, M.-H.; Park, J.-H.; Lee, Y.-J.; Choi, Y.-C.; Park, J. C.; Chun, D. H. Alcohol and Water Free Synthesis of Mesoporous Silica Using Deep Eutectic Solvent as a Template and Solvent and Its Application as a Catalyst Support for Formic Acid Dehydrogenation. *ACS Sustainable Chem. Eng.* **2018**, *6*, 12241−12250.
(56) Cano-Franco, J. C.; Álvarez-Láinez, M. Effect of CeO_2 Content in Morphology and Optoelectronic Properties of TiO_2-CeO_2 Nanoparticles in Visible Light Organic Degradation. *Mater. Sci. Semicond. Process.* **2019**, *90*, 190−197.
(57) Artiglia, L.; Orlando, F.; Roy, K.; Kopelent, R.; Safonova, O.; Nachtegaal, M.; Huthwelker, T.; Van Bokhoven, J. A. Introducing Time Resolution to Detect Ce^{3+} Catalytically Active Sites at the Pt/CeO_2 Interface through Ambient Pressure X-ray Photoelectron Spectroscopy. *J. Phys. Chem. Lett.* **2017**, *8*, 102−108.
(58) Kato, S.; Ammann, M.; Huthwelker, T.; Paun, C.; Lampimäki, M.; Lee, M. T.; Rothensteiner, M.; Van Bokhoven, J. A. Quantitative Depth Profiling of Ce^{3+} in Pt/CeO_2 by in Situ High-Energy XPS in a Hydrogen Atmosphere. *Phys. Chem. Chem. Phys.* **2015**, *17*, 5078−5083.
(59) Nie, L.; Mei, D.; Xiong, H.; Peng, B.; Ren, Z.; Hernandez, X. I. P.; DeLaRiva, A.; Wang, M.; Engelhard, M. H.; Kovarik, L.; Datye, A. K.; et al. Activation of Surface Lattice Oxygen in Single-Atom Pt/CeO_2 for Low-Temperature CO Oxidation. *Science* **2017**, *358*, 1419−1423.
(60) Yousaf, A. B.; Imran, M.; Uwitonze, N.; Zeb, A.; Zaidi, S. J.; Ansari, T. M.; Yasmeen, G.; Manzoor, S. Enhanced Electrocatalytic Performance of Pt_3Pd_1 Alloys Supported on CeO_2/C for Methanol Oxidation and Oxygen Reduction Reactions. *J. Phys. Chem. C* **2017**, *121*, 2069−2079.
(61) Neitzel, A.; Figueroba, A.; Lykhach, Y.; Skála, T.; Vorokhta, M.; Tsud, N.; Mehl, S.; Ševčíková, K.; Prince, K. C.; Neyman, K. M.; et al. Atomically Dispersed Pd, Ni, and Pt Species in Ceria-Based Catalysts: Principal Differences in Stability and Reactivity. *J. Phys. Chem. C* **2016**, *120*, 9852−9862.
(62) Kundu, S.; Ciston, J.; Senanayake, S. D.; Arena, D. A.; Fujita, E.; Stacchiola, D.; Barrio, L.; Navarro, R. M.; Fierro, J. L. G.; Rodriguez, J. A. Exploring the Structural and Electronic Properties of Pt/Ceria-Modified TiO_2 and Its Photocatalytic Activity for Water Splitting under Visible Light. *J. Phys. Chem. C* **2012**, *116*, 14062−14070.
(63) Huang, W.; Wang, H.; Zhou, J.; Wang, J.; Duchesne, P. N.; Muir, D.; Zhang, P.; Han, N.; Zhao, F.; Zeng, M.; Zhong, J.; et al. Highly Active and Durable Methanol Oxidation Electrocatalyst Based on the Synergy of Platinum-Nickel Hydroxide-Graphene. *Nat. Commun.* **2015**, *6*, 10035−10043.
(64) Lang, Z.; Zhuang, Z.; Li, S.; Xia, L.; Zhao, Y.; Zhao, Y.; Han, C.; Zhou, L. MXene Surface Terminations Enable Strong Metal-Support Interactions for Efficient Methanol Oxidation on Palladium. *ACS Appl. Mater. Interfaces* **2020**, *12*, 2400−2406.
(65) Zhang, D.; Zhang, C.; Chen, Y.; Wang, Q.; Bian, L.; Miao, J. Support Shape Effect on the Catalytic Performance of Pt/CeO2 Nanostructures for Methanol Electrooxidation. *Electrochimica Acta* **2014**, *139*, 42−47.
(66) Guo, D. J.; Jing, Z. H. A Novel Co-Precipitation Method for Preparation of Pt-CeO2 Composites on Multi-Walled Carbon Nanotubes for Direct Methanol Fuel Cells. *J. Power Sources* **2010**, *195*, 3802−3805.
(67) He, Q.; Shen, Y.; Xiao, K.; Xi, J.; Qiu, X. Alcohol Electro-Oxidation on Platinum−Ceria/Graphene Nanosheet in Alkaline Solutions. *Int. J. Hydrogen Energy* **2016**, *41*, 20709−20719.
(68) Farias, M. J. S.; Herrero, E.; Feliu, J. M. Site Selectivity for CO Adsorption and Stripping on Stepped and Kinked Platinum Surfaces in Alkaline Medium. *J. Phys. Chem. C* **2013**, *117*, 2903−2913.
(69) Wang, W.; Zhang, J.; Wang, F.; Mao, B. W.; Zhan, D.; Tian, Z. Q. Mobility and Reactivity of Oxygen Adspecies on Platinum Surface. *J. Am. Chem. Soc.* **2016**, *138*, 9057−9060.
(70) Wang, X.; Xie, M.; Lyu, F.; Yiu, Y. M.; Wang, Z.; Chen, J.; Chang, L. Y.; Xia, Y.; Zhong, Q.; Chu, M.; et al. Bismuth Oxyhydroxide-Pt Inverse Interface for Enhanced Methanol Electrooxidation Performance. *Nano Lett.* **2020**, *20*, 7751−7759.
(71) Blyholder, G. Molecular Orbital View of Chemisorbed Carbon Monoxide. *J. Phys. Chem.* **1964**, *68*, 2772−2777.

https://doi.org/10.1021/acs.jpcc.2c05069
J. Phys. Chem. C 2022, 126, 18670−18682